Bulletin of the Seismological Society of America, Vol. 94, No. 6B, pp. S175–S189, December 2004

Constraining the Slip Distribution and Fault Geometry of the M_w 7.9, 3 November 2002, Denali Fault Earthquake with Interferometric Synthetic Aperture Radar and Global Positioning System Data

by Tim J. Wright, Zhong Lu, and Chuck Wicks

Abstract The M_w 7.9, Denali fault earthquake (DFE) is the largest continental strike-slip earthquake to occur since the development of Interferometric Synthetic Aperture Radar (InSAR). We use five interferograms, constructed using radar images from the Canadian Radarsat-1 satellite, to map the surface deformation at the western end of the fault rupture. Additional geodetic data are provided by displacements observed at 40 campaign and continuous Global Positioning System (GPS) sites. We use the data to determine the geometry of the Susitna Glacier fault, thrusting on which initiated the DFE, and to determine a slip model for the entire event that is consistent with both the InSAR and GPS data. We find there was an average of 7.3 $\pm$ 0.4 m slip on the Susitna Glacier fault, between 1 and 9.5 km depth on a 29 km long fault that dips north at 41 $\pm$ 0.7° and has a surface projection close to the mapped rupture. On the Denali fault, a simple model with large slip patches finds a maximum of 8.7 $\pm$ 0.7 m of slip between the surface and 14.3 $\pm$ 0.2 km depth. A more complex distributed slip model finds a peak of 12.5 $\pm$ 0.8 m in the upper 4 km, significantly higher than the observed surface slip. We estimate a geodetic moment of 670 $\pm$ 10 $\times$ 10^{18} N m (M_w 7.9), consistent with seismic estimates. Lack of preseismic data resulted in an absence of InSAR coverage for the eastern half of the DFE rupture. A dedicated geodetic InSAR mission could obviate coverage problems in the future.

Introduction

The magnitude 7.9 earthquake that struck central Alaska on 3 November 2002 was one of the largest earthquakes to break continental crust in the instrumental period, and the largest strike-slip earthquake in North America in more than 150 years. The earthquake ruptured about 300 km of the Denali fault system (Fig. 1), with right-lateral offsets of up to 9 m observed at the surface (Eberhart-Phillips *et al.*, 2003). The rupture initiated with slip on a previously unknown thrust fault, the ~40 km long Susitna Glacier fault (SGF). The rupture propagated eastward for about 220 km along the right-lateral Denali fault where right-lateral surface slip averaged ~5 m, before stepping southeast onto the Totschunda fault for about 70 km, where offsets were less than 2 m (Haeussler *et al.*, 2004).

The Trans-Alaska Pipeline (Fig. 1), crossing the Denali fault toward the western end of the rupture, survived the earthquake, thanks to insightful seismotectonic studies and engineering in the 1970s (Eberhart-Phillips *et al.*, 2003). The earthquake produced thousands of landslides, clustered within a 30-km-wide swath straddling the rupture zones along the Denali and Totschunda faults (Fuis and Wald, 2003). The earthquake also triggered numerous small shocks at many volcanic centers as far as 3600 km away (Eberhart-Phillips *et al.*, 2003).

The 3 November Denali fault earthquake (DFE) was preceded by a magnitude 6.7 shock on 23 October 2002, the Nenana Mountain earthquake (NME), a pure strike-slip earthquake, which was located on the Denali fault, immediately to the west of the DFE rupture (Fig. 1). The NME increased the Coulomb stress at the future hypocenter of the DFE by 30–60 kPa, for thrust faults oriented parallel to the Susitna Glacier fault (Anderson and Ji, 2003; Wright *et al.*, 2003).

Lu *et al.* (2003) presented preliminary analysis of a few interferograms that covered the NME and DFE. Wright *et al.* (2003) described a more detailed study of the NME. In this article, we present additional Interferometric Synthetic Aperture Radar (InSAR) data that help determine the fault geometry and slip distribution of the 3 November 2002 DFE. To complement the InSAR data, which only has coverage for the western rupture (Fig. 1), we use 40 coseismic GPS displacements from Hreinsdóttir *et al.* (2003).

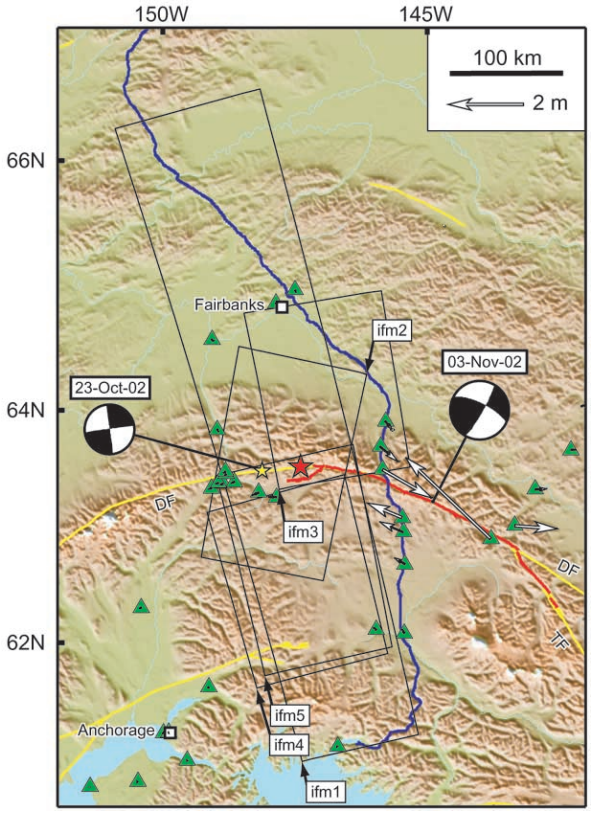

Figure 1. Topographic and tectonic map of the region surrounding the 2002 Denali fault earthquakes. Yellow lines show previously mapped faults and the red line is the mapped rupture of the 3 November 2002 earthquake. Focal mechanisms are from Harvard Centroid Moment Tensor; the yellow and red stars indicate the epicenters of the 23 October and 3 November mainshocks respectively (Alaska Earthquake Information Center). Black lines delimit the extents of the InSAR data used for this study, and white arrows are displacements observed with GPS. The blue line marks the route of the Trans-Alaskan oil pipeline. DF, Denali fault; TF, Totschunda fault.

Interferometric Synthetic Aperture Radar Data

Since the launch of ERS-1 in 1991, InSAR has become a widely used technique for mapping deformation of the Earth's surface. By differencing the phase measurements from two radar images acquired at different times, maps of crustal deformation can be obtained with a precision of a few millimeters and a spatial resolution of a few tens of meters (Massonnet and Feigl, 1998). InSAR has been used to study the coseismic deformation of more than 30 continental earthquakes, as well as interseismic and postseismic strain over several earthquake-prone areas (e.g., Bürgmann *et al.*, 2000; Wright, 2002). Almost all previous studies have used data from the European satellites ERS-1 and ERS-2. However, recently acquired data from ERS-2 that cover the time of the Denali earthquake can only form pairs with large Doppler centroid differences and/or large orbital baselines, which makes forming a coherent interferogram impossible. Unusually, the western end of the Denali fault is covered by a large number of synthetic aperture radar (SAR) images acquired by the Canadian Radarsat-1 satellite (Parashar *et al.*, 1993), archived at the Alaska SAR Facility.

The Radarsat-1 repeat time of 24 days is shorter than the 35-day primary repeat-cycle for ERS-1 and ERS-2. Unlike ERS-1 and ERS-2, which have a fixed incidence angle of about 23°, Radarsat-1 can operate with a variety of imaging modes, with possible incidence angles ranging from 20° to 60° (Parashar *et al.*, 1993). This enables a target area to be revisited more frequently than the nominal 24-day repeat. In standard beam mode, Radarsat-1 has a slant range pixel spacing of ~8.1 m and a resolution of ~12 m. The azimuth pixel spacing is ~5.3 m (resolution ~8.6 m). We take two looks in the slant range direction and seven in the azimuth direction. The interferograms are geocoded on a regular 40-m grid.

Interferometric processing for Radarsat-1 SAR is slightly different from that for ERS-1 or pre-2001 ERS-2, and some additional care is required. Firstly, not every image pair with a temporal separation of 24 days can be processed into an interferogram. A candidate interferometric pair should have not only a baseline suitable for deformation measurement, but also an identical imaging mode. Secondly, the accuracy of the satellite restitute vectors provided in Radarsat-1 metadata is poorer than the precision vectors for ERS-1 and ERS-2. Therefore, the baseline of the interferometric pair must be improved. We refined the baseline (horizontal and vertical components, as well as the rate of horizontal and vertical components over the time interval) using known elevation heights via a least-squares approach. By assuming the displacement over the very far-field is negligible, the terrain heights from a digital elevation model (DEM) near the azimuthal ends of the SAR images are extracted to refine the baseline. Despite this refinement, some residual phase ramps from orbital errors can remain in the interferograms. Thirdly, unlike the ERS-1 and ERS-2 satellites, which employed yaw-steering of the SAR to maintain the Doppler centroid with small variations (at least until mid-2001), Radarsat-1 nominally operates with a broadside imaging geometry, and the Doppler centroid therefore varies significantly with latitude. This makes it difficult to process multiple SAR frames simultaneously with a conventional range-Doppler SAR processor. Where possible, we have concatenated multiple SAR frames together to form interferograms up to 600 km long, centered on the Denali fault. In cases where there were large along-track variations in Doppler centroid values, we processed the data using a SAR processor (Bamler, 1992) that takes into account the along-track variation of Doppler centroid (Joughin, 2002; Gamma Remote Sensing Research and Consulting AG, 2003)

We have used five Radarsat-1 interferograms (ifms) to map the coseismic displacements associated with the 3 November 2002 DFE. The image acquisition times and asso-

ciated imaging parameters are shown in Table 1. We used the two-pass InSAR method (Massonnet and Feigl, 1998) with the U.S. Geological Survey (USGS) 15-minute Alaska DEM to correct for the topographic contribution to the observed phase values. The DEM has a specified horizontal accuracy of ~60 m and root-mean-square vertical error of ~15 m, resulting in no more than 7 mm (1σ) line-of-sight error in the interferogram with the largest perpendicular baseline (ifm3) (Table 1). The interferograms were acquired on a mixture of ascending and descending passes and span intervals of 24 or 48 days. Unfortunately, three of our interferograms (ifm3, ifm4, ifm5) only span half of the deformation field. This is because the Radarsat-1 beam mode in the pre-earthquake data changes at the location where we lose data. Switching beam modes results in a data gap of more than 100 km for Radarsat.

The interferograms are surprisingly coherent (Fig. 2), except for glaciated areas with high relief within 5–10 km of the fault rupture. They reveal range changes of up to ± 0.6 m close to the fault, with most of the deformation concentrated within 100 km of the observed rupture. Apart from ifm1, our interferograms image the deformation of both the NME and DFE. To remove this relatively small signal, we calculated synthetic interferograms for the viewing geometries of our interferograms based on the distributed-slip, elastic dislocation model of the NME presented by Wright *et al.* (2003), which was well determined using six different interferograms. The synthetic interferograms were then subtracted from our data, leaving only the signal from the DFE.

Each interferogram shows the component of the three-dimensional surface displacement vector in the satellite line of sight. The effect of this is most evident in the difference between ifm1, acquired on an ascending satellite pass, and ifm2, acquired on a descending pass (Table 1; Fig. 3). The interferograms have a similar sensitivity to vertical motion, but eastward displacements result in range increases in the ascending interferogram (ifm1) and range decreases in the descending interferogram (ifm2). This causes marked differences between the two interferograms in the area of the Susitna Glacier fault (SGF) (Fig. 3)—ifm2 seems relatively simple, with relative range increases south of the fault and range decreases to its north. In contrast, ifm1 shows a complex pattern, with an anomalous relative range increase immediately south of the SGF, compared to range decreases elsewhere south of the Denali fault. North of the westward projection of the SGF rupture, but south of the Denali fault, ifm1 shows a range decrease, and north of the Denali fault there are range increases. These patterns can only be explained if there is subsidence immediately south of the SGF that is larger (in ascending ifm1) than the range decreases caused by the westward motion generally expected south of the Denali fault. In descending ifm2, which is less coherent in the near-fault area, any range increase from the subsidence is hidden within the range increase due to the westward motion south of the Denali fault, or in the incoherent area. Additional evidence supporting subsidence as well as horizontal deformation in this location is that the range increase south of the SGF in ifm2 reaches a maximum of 600 mm, nearly double the range decrease in ifm1. Similarly, the range decrease in ifm1 between the surface trace of the Denali fault and the westward projection of the SGF is consistent with uplift in that location. To explain these vertical motions requires the SGF to be a thrust fault, dipping north. This is consistent with the first-motion focal mechanism and field observations, which suggested the DFE initiated on a thrust fault (Eberhart-Phillips *et al.*, 2003).

Table 1
Interferograms Constructed for This Study

	Date 1	Date 2	θ*	$\alpha^{\dagger}$	$B_{\perp}{}^{\ddagger}$
ifm1	29-Oct-02	22-Nov-02	27.7	−14.5	110
ifm2	20-Oct-02	13-Nov-02	39.5	−169.1	−10
ifm3	11-Oct-02	4-Nov-02	47.0	−9.1	158
ifm4	18-Sept-02	5-Nov-02	23.4	−15.3	22
ifm5	15-Oct-02	8-Nov-02	34.2	−12.3	105

*Incidence angle at scene center.
†Satellite Azimuth (angle between the satellite ground track and local north).
‡Perpendicular baseline (in meters).

Global Positioning System Data

In addition to the InSAR data, 40 displacement vectors measured using the Global Positioning System (GPS) recorded the coseismic displacements of the DFE (Hreinsdóttir *et al.*, 2003). These data consisted of 28 campaign GPS sites and 12 permanent GPS sites and were mostly surveyed within one week after the earthquake. Details of the methods used to determine displacement vectors from these data are described by Hreinsdóttir *et al.* (2003).

The GPS vectors (Fig. 1) are consistent with predominantly right-lateral motion during the earthquake. The largest observed displacement is 3.1 m at MEN, ~5 km south of the fault, toward the eastern end of the rupture. Although the data are sparse compared to the InSAR data, they have the advantage of comprising three components of the deformation field. Furthermore, some GPS data are available in the eastern half of the deformation field, where there is no InSAR coverage (Fig. 1).

Modeling

We use the InSAR and GPS data to determine a simple fault model, consisting of uniform slip on a few rectangular fault planes, and a more complex model in which slip was allowed to vary across the fault planes. To make the inversions manageable, we subsample the InSAR data using the Quadtree algorithm (e.g., Jónsson *et al.*, 2002). In this scheme, the unwrapped interferograms are divided into quadrants. If the variance with each quadrant exceeds a specified threshold (equal to 6 radians^2 in our case), the quadrant

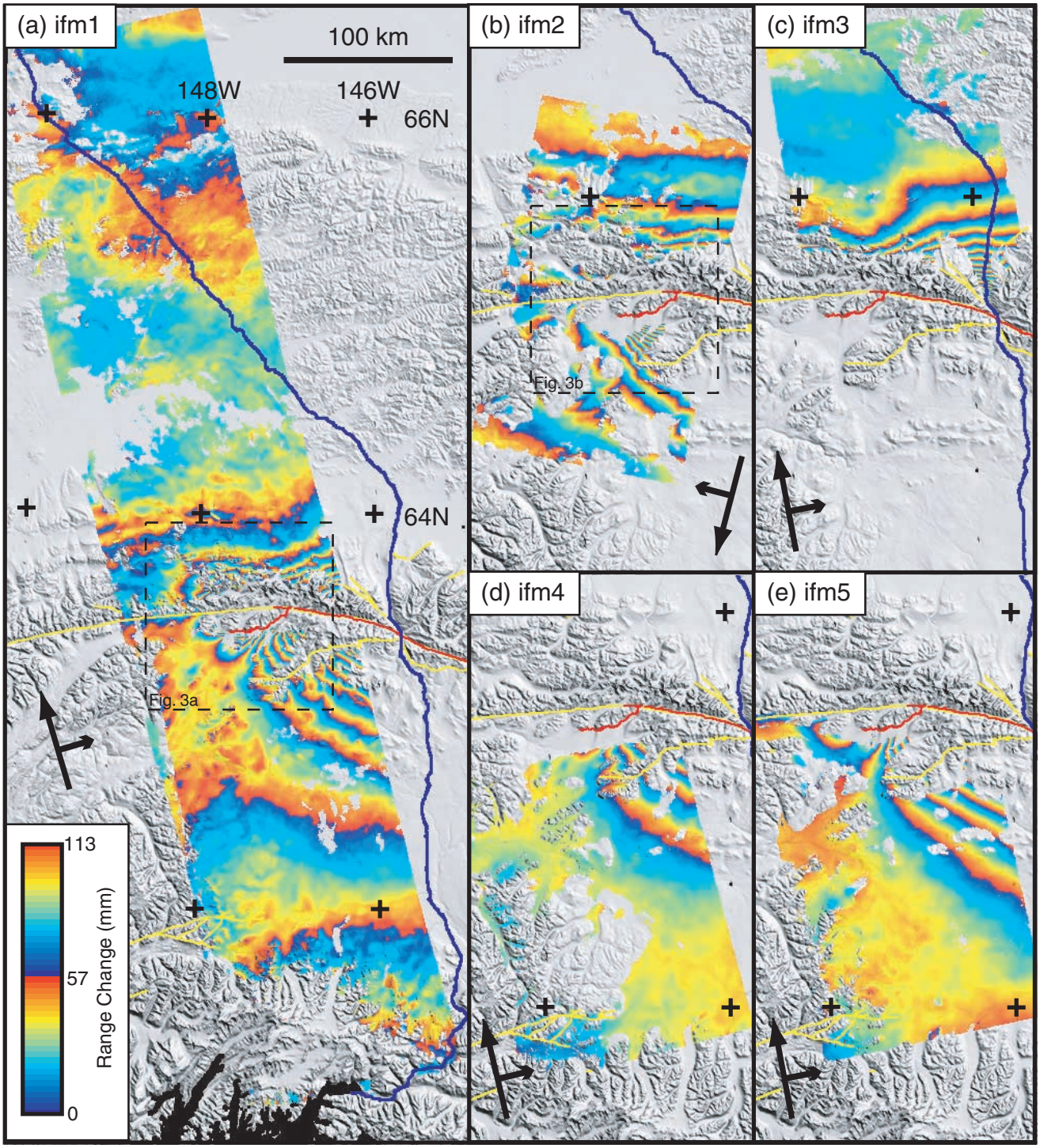

Figure 2. Radarsat-1 interferograms constructed for the 3 November 2002 DFE (Table 1). The data are unwrapped and plotted rewrapped with a ~57 mm (4π radians) interval. Warm colors indicate motion toward the satellite, whose along-track and look directions are shown by the large and small black arrows, respectively. Gray areas show shaded relief from the USGS 60-m DEM of the area. Gaps in the InSAR coverage indicate areas that we have been unable to unwrap successfully. Coseismic deformation due to the NME has been removed from ifm2-5, using the model of Wright *et al.* (2003). Yellow lines, mapped faults; red lines, 3 November 2002 rupture; blue line, pipeline. All subfigures are plotted on the same scale, and tick marks are given at 2° intervals.

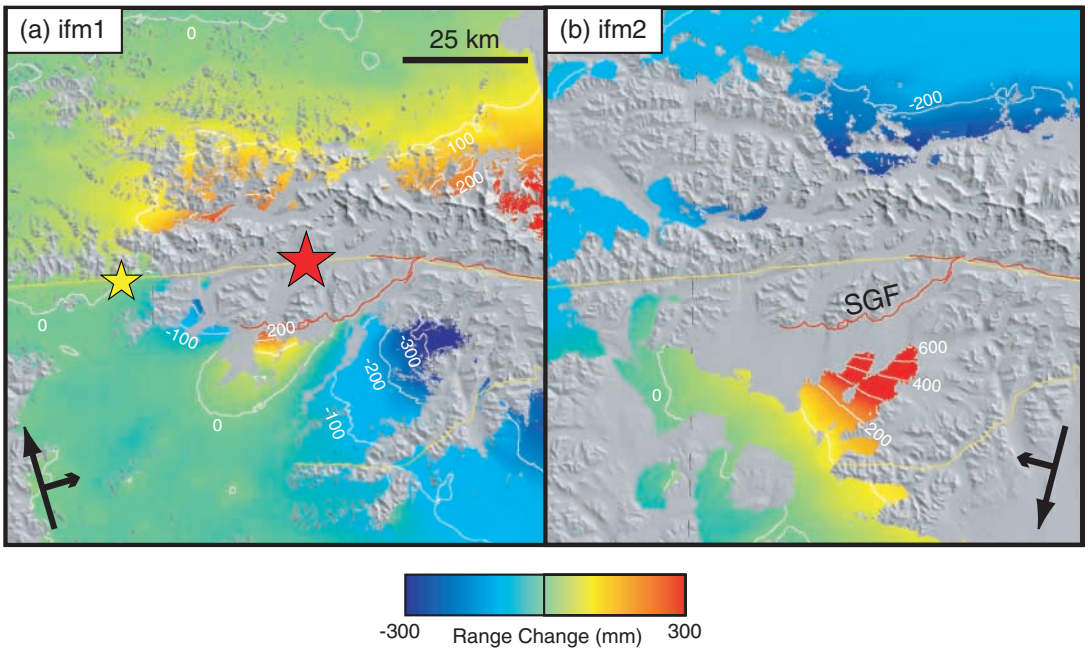

Figure 3. Close-up view of the unwrapped phase in (a) ascending ifm1 and (b) descending ifm2 in the area of the Susitna Glacier fault (SGF). White contours are shown for every 100 mm of range change. The yellow and red stars indicate the epicenters of the NME and DFE, respectively. The extents of the figure are given as a dashed box in Figure 2a.

is subdivided into four. This process is repeated until either the variance within the quadrant is less than the threshold, or the quadrant reaches a minimum block diameter, specified at 640 m for these data. In addition, a maximum block size of 10 km is used. This length scale is chosen because it represents a typical correlation length scale for atmospheric noise (e.g., Wright *et al.*, 2003). After subsampling, the $\sim 10^7$ phase observations in the original interferograms are reduced to a total of 4940. Because of the high degree of spatial correlation in InSAR data (e.g., Hanssen, 2001), little information is lost in this process.

Nine-Segment Model

Initially we solve for a relatively simple model that satisfies the InSAR and GPS data. For the main Denali fault we fix the geometry using eight of the nine simplified fault planes parameterised by Hreinsdóttir *et al.* (2003) that coincide with the mapped surface rupture. We do not use their westernmost segment, which did not rupture the surface in this earthquake or have significant slip at depth in their model. We force slip on these segments to be pure right-lateral strike-slip and assume the faults are vertical. We solve for the slip on each patch, and a single lower depth extent, applied to all eight patches. Simultaneously, we solve completely for the fault geometry and slip on the SGF. In addition, line-of-sight offsets and linear ramps are determined for each interferogram to account for any unmodeled orbital errors in the original data sets.

We use a hybrid linear/nonlinear inversion algorithm to carry out the inversion. This procedure solves the linear equations for the slip on fault patches and the Helmert parameters (ramps and offsets in interferograms) and uses a bounded nonlinear downhill simplex algorithm to solve for the remaining parameters that mostly describe fault geometry (Wright *et al.*, 1999). Local minima are avoided by restarting the inversion from many different initial fault geometries. Parameter errors were determined using Monte Carlo simulation of correlated noise. In this method, multiple sets of correlated noise are simulated for the InSAR data. This is based on an exponential 1D covariance function that has a variance of 100 mm^2 and falls to 1/e of the variance at a distance of 15 km—typical values for InSAR data. For the campaign GPS data we assume uncorrelated noise with a standard deviation of 10 mm for the horizontal components and 30 mm for the vertical component. Although GPS data noise is almost certainly spatially correlated, the exact form of the correlation in this case is unknown. Furthermore, most GPS observations are separated by many kilometers, reducing the effects of correlation. Our GPS uncertainties are probably overcautious but reflect uncertainties in corrections for preseismic and postseismic velocities at the sites. For the 12 campaign GPS sites, we use smaller errors of 2 mm and 6 mm for the horizontal and vertical errors, respectively. One hundred noise simulations are added to the original data sets; parameter errors are then determined from the distribution of the best-fit solutions to each of these noisy data sets.

The model places between 0 and 8.7 m of slip on the

strike-slip section of the Denali fault (Table 2), with a fairly smooth transition in slip values between the segments. The maximum slip is 8.7 ± 0.7 m, 30 km east of the pipeline crossing. This inversion does not place any slip on the easternmost segment, along the Totschunda fault. The best-fit single depth for the strike-slip segments is 14.3 ± 0.2 km. For the SGF, we find that 7.3 ± 0.4 m of pure thrusting is preferred between 1.2 ± 0.3 and 9.5 ± 0.3 km depth on a fault that is 28.5 ± 0.6 km long and dips north at 41 ± 0.7°. The surface projection of the model fault plane is very close to the observed fault trace. The total geodetic moment is 650 ± 8 × 10^{18} N m (M_w ~7.9), of which 90 × 10^{18} N m comes from the SGF—equivalent to a M_w ~7.3 earthquake in its own right. This is consistent with estimates from seismology (e.g., Eberhart-Phillips *et al.*, 2003; Tsuboi *et al.*, 2003; Dreger *et al.*, 2004).

The model provides a reasonable fit to the InSAR data (Figs. 2 and 4), and the InSAR residuals are generally small (Fig. 5) (rms misfit = 3.1 cm). However, the displacement observed at GPS point MEN, which is the closest GPS observation to the fault and also the largest observed GPS displacement, is particularly poorly fit, with a misfit of 0.7 m in the horizontal component of displacement at that location (Fig. 6). Several other near-fault GPS displacements are also poorly fit by this simple model, and the overall rms misfit is 8.4 cm for the horizontal GPS components and 5.4 cm for the vertical component.

Distributed-Slip Model

To improve the fit to the data, we further subdivided our original fault segments into small patches. The strike-slip segments were extended to a depth of 16 km. The geometry of the SGF was fixed to the best-fit geometry determined earlier but extended so that slip could occur between the surface and a depth of 10 km. In total, we solved for slip on 312, ~4 by 4 km fault patches. To determine the earthquake slip model, vector **m**, for the specified fault geometry, we set up the following equation:

$$\begin{pmatrix} \mathbf{A} & \mathbf{x} & \mathbf{y} & 1 \\ \gamma^2\nabla^2 & 0 & 0 & 0 \end{pmatrix} \begin{pmatrix} \mathbf{m} \\ a \\ b \\ c \end{pmatrix} = \begin{pmatrix} \mathbf{d} \\ 0 \end{pmatrix}, \quad (1)$$

where **A** is a matrix containing Green's functions (displacements calculated at the observation locations, **x** and **y**, for 1 m of slip on each fault patch using the elastic dislocation formulation of Okada (1985) and projected into the satellite line of sight for the InSAR data); ∇^2 is the finite difference approximation of the Laplacian operator, which acts to smooth the slip distribution, the importance of which is governed by the size of the scalar smoothing factor γ^2; a and b are phase gradients in the x- and y-directions, respectively; c is a line-of-sight offset accounting for the unknown zero-phase level; and **d** is a vector containing the observed displacements. A zero-slip boundary condition is imposed around the fault, except for the upper surface.

We constructed a full variance-covariance matrix (VCM) for each geodetic data set, including off-diagonal terms for the InSAR observations, using the 1D covariance function discussed previously. This enables the observations to be correctly weighted; an upper triangular weight matrix **W** can be constructed from the Cholesky decomposition of the inverse of the VCM ($\mathbf{W^TW} = \mathbf{\Sigma}^{-1}$) (e.g., Strang and Borre, 1997). Equation (1) therefore becomes

$$(\mathbf{W}\ 1)\begin{pmatrix} \mathbf{A} & \mathbf{x} & \mathbf{y} & 1 \\ \gamma^2\nabla^2 & 0 & 0 & 0 \end{pmatrix} \begin{pmatrix} \mathbf{m} \\ a \\ b \\ c \end{pmatrix} = (\mathbf{W}\ 1)\begin{pmatrix} \mathbf{d} \\ 0 \end{pmatrix}. \quad (2)$$

In practice, because we have five independent interfer-

Table 2
Source Parameters for the Nine-Segment Model

	SGF*	D1†	D2	D3	D4	D5	D6	D7	D8
Strike	249.6 ± 0.7°	98.3°	105.1°	119.0°	108.4°	114.9°	116.8°	151.2°	135.3°
Dip	41.0 ± 0.7°	90°							
Rake	84.6 ± 1.3°	180°							
Slip (m)	7.3 ± 0.4	2.4 ± 0.1	5.7 ± 0.1	5.0 ± 0.2	8.7 ± 0.7	5.8 ± 0.6	7.5 ± 0.1	2.9 ± 0.4	0 ± 0‡
Depth to Top (km)	1.3 ± 0.3	0							
Depth to Bottom (km)	9.5 ± 0.3	14.3 ± 0.2							
Fault Length (km)	28.5 ± 0.6	47.0	20.3	22.2	31.6	39.6	51.5	20.8	49.7
X-coodinate§ (km)	481.8 ± 0.3	512.4	545.5	565.0	589.7	622.7	663.6	691.6	714.1
Y-coordinate (km)	7036.1 ± 0.3	7042.1	7036.1	7028.0	7017.7	7004.4	6984.5	6963.8	6937.0
Moment (10^{18} N m)	650 ± 8								

Parameters without error bars were held fixed in the inversion.

*SGF, Susitna Glacier fault.

†D, Denali fault. Segments D1–D8 are the geometries defined by Hreinsdóttir *et al.* (2003).

‡Inversion of all noisy data sets estimated 0 m of slip on this segment, hence the formal error is 0 m. This indicates that the best-fit slip is strictly negative (left-lateral) on this segment.

§Coordinates are in UTM Zone 6.

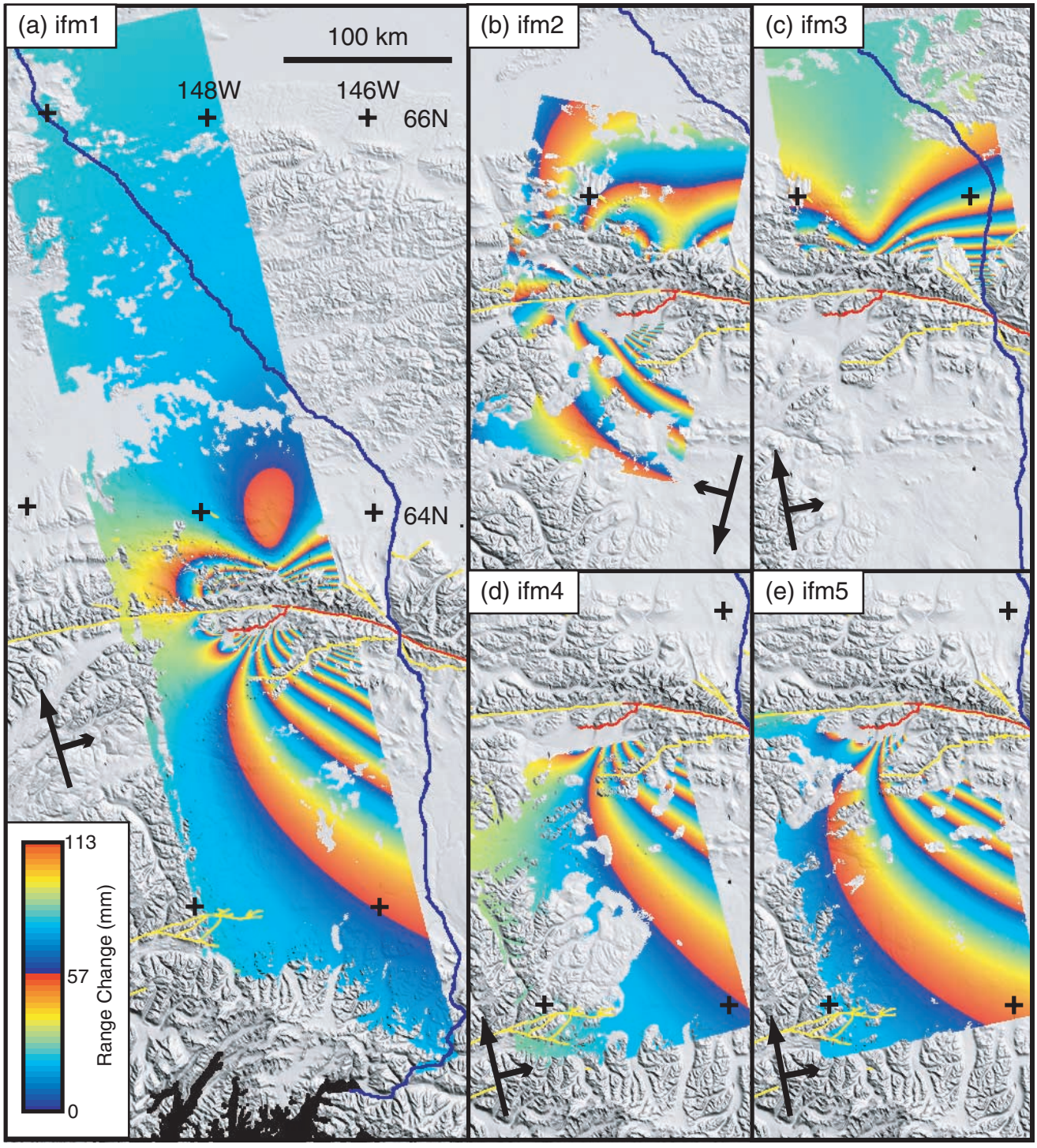

Figure 4. Synthetic interferograms generated by projecting the predictions of our nine-segment fault model into the satellite line of sight for each interferogram. All other features are as defined in Figure 2.

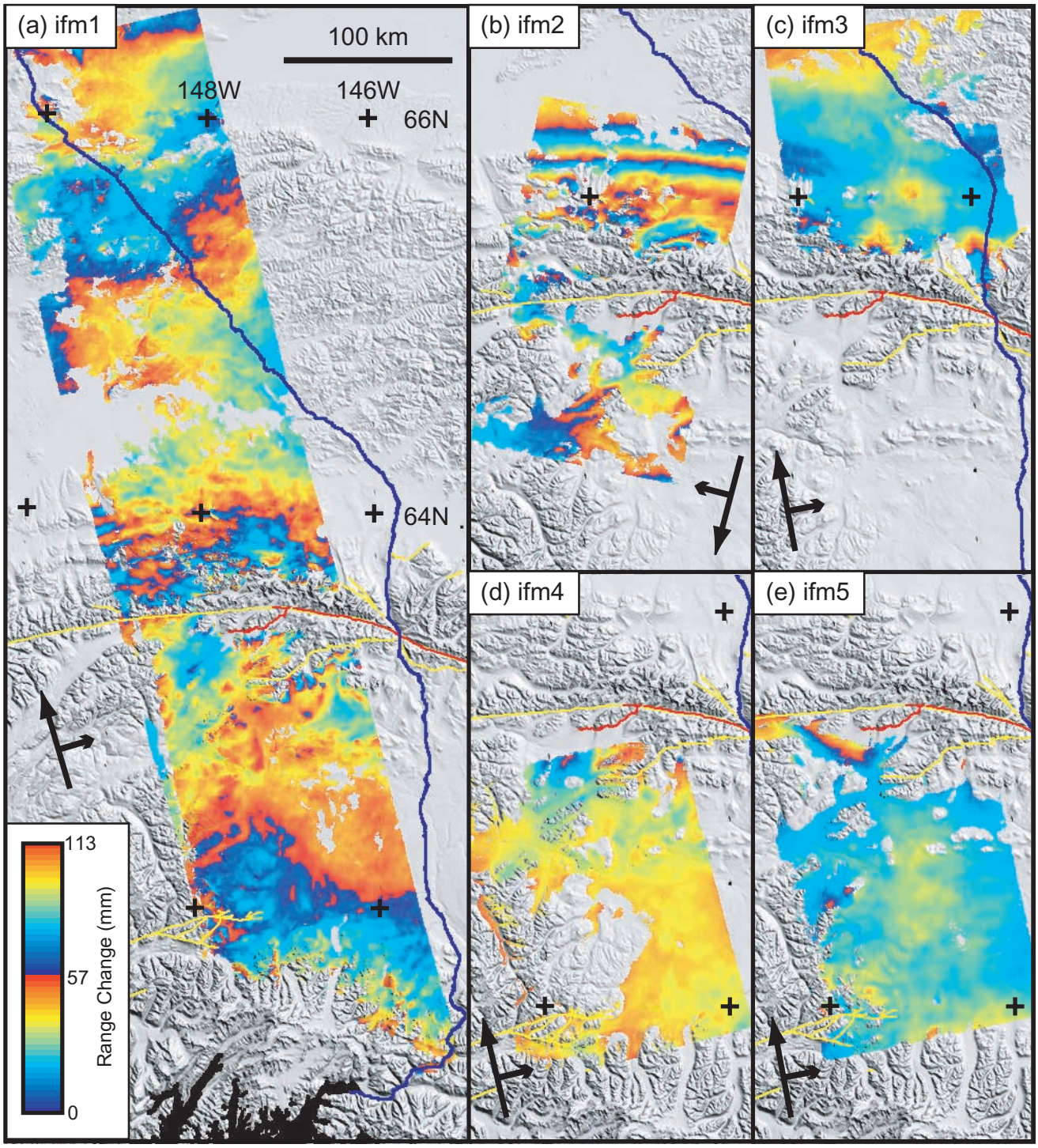

Figure 5. Residual interferograms for our nine-segment fault model, generated by subtracting the model interferograms (Fig. 4) from the observed data (Fig. 2). Estimated linear orbital ramps have been removed. Other features are as defined in Figure 2.

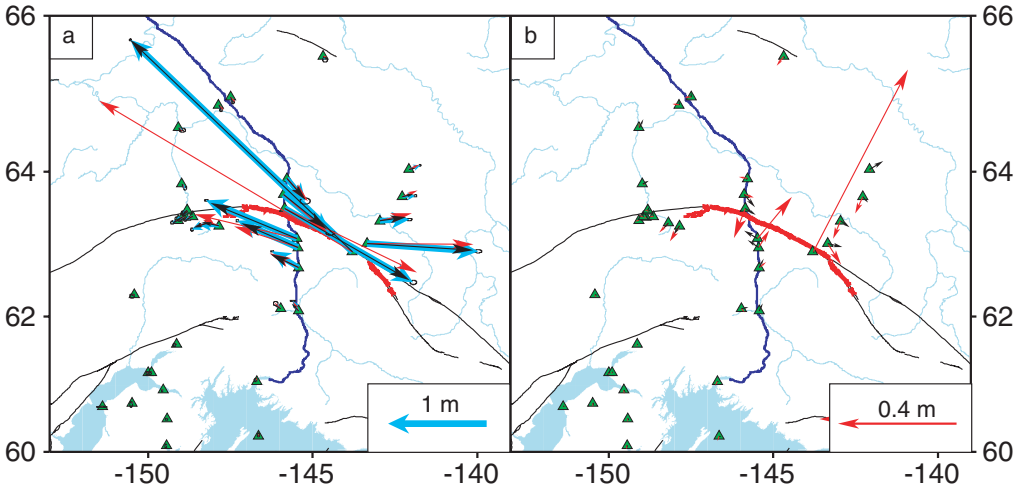

Figure 6. (a) Observed and modeled GPS data for the Denali fault earthquake (DFE). Cyan arrows are the observed displacements, measured at each of locations marked by a green triangle. Red arrows are the displacements predicted by the nine-segment fault model, and black arrows are the predictions of the distributed slip model. (b) Residual displacements for the nine-segment (red arrows) and distributed slip (black arrows) models. Note the large misfit at site MEN for the nine-segment model. Black lines, mapped faults; red line, 3 November rupture; dark blue line, pipeline; cyan lines, rivers/ocean.

ograms and a set of GPS observations, equation (2) must be modified to take into account additional nuisance parameters. To illustrate this process, the unweighted equation for two data sets is

$$\begin{pmatrix} \mathbf{A}_1 & \mathbf{x}_1 & \mathbf{y}_1 & 1 & 0 & 0 & 0 \\ \mathbf{A}_2 & 0 & 0 & 0 & \mathbf{x}_2 & \mathbf{y}_2 & 1 \\ \gamma^2\nabla^2 & 0 & 0 & 0 & 0 & 0 & 0 \end{pmatrix} \begin{pmatrix} \mathbf{m} \\ a_1 \\ b_1 \\ c_1 \\ a_2 \\ b_2 \\ c_2 \end{pmatrix} = \begin{pmatrix} \mathbf{d}_1 \\ \mathbf{d}_2 \\ 0 \end{pmatrix}, \qquad (3)$$

where the subscripts correspond to the data set number. These equations are weighted by multiplying the first and second rows of the design and observation matrices by weight matrices $\mathbf{W}_1$ and $\mathbf{W}_2$ respectively. The additional data sets are easily incorporated by adding additional rows to the design matrix in equation (3). Note that we do not solve for nuisance parameters for the GPS data, and assume that reference frame issues have been dealt with correctly by Hreinsdóttir *et al.* (2003).

We solve for the best smooth fault slip $\mathbf{m}$ and nuisance parameters a, b, and c using a two-stage process. Initially we solve for both slip and nuisance parameters using a standard linear least-squares approach (e.g., Menke, 1989). The values of the nuisance parameters are then fixed, and we repeat the inversion using the nonlinear fast non-negative least squares algorithm (FNNLS) (Bro and De Jong, 1997). As the name implies, FNNLS places a positivity constraint on fault slip.

The best-fit slip distribution depends on the size of the smoothing factor γ^2. High values will lead to an oversmooth solution with large misfit; low values result in small misfits, but oscillating slip distributions. Because the size of γ^2 required varies when different data sets, weight matrices, and fault geometries are used, we define a new parameter, solution roughness ρ, the mean, absolute Laplacian of the slip model (e.g., Jónsson *et al.*, 2002),

$$\rho = \|\nabla^2\mathbf{m}\|_{L1}. \qquad (4)$$

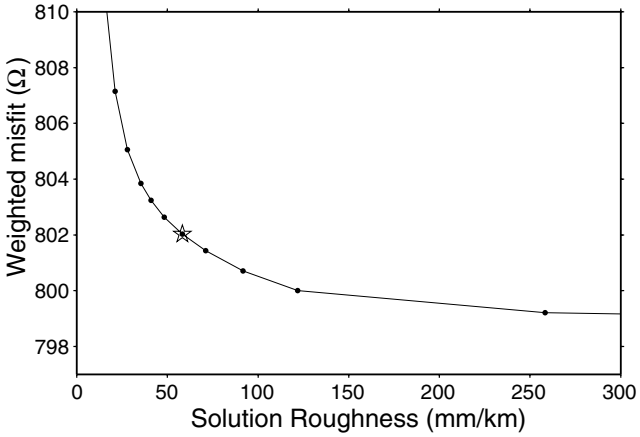

Figure 7. Tradeoff between weighted misfit function Ω and the solution roughness for the distributed-slip, joint-inversion model. Each solid dot represents an individual experiment, and the star is the compromise solution selected and shown in Figure 8a.

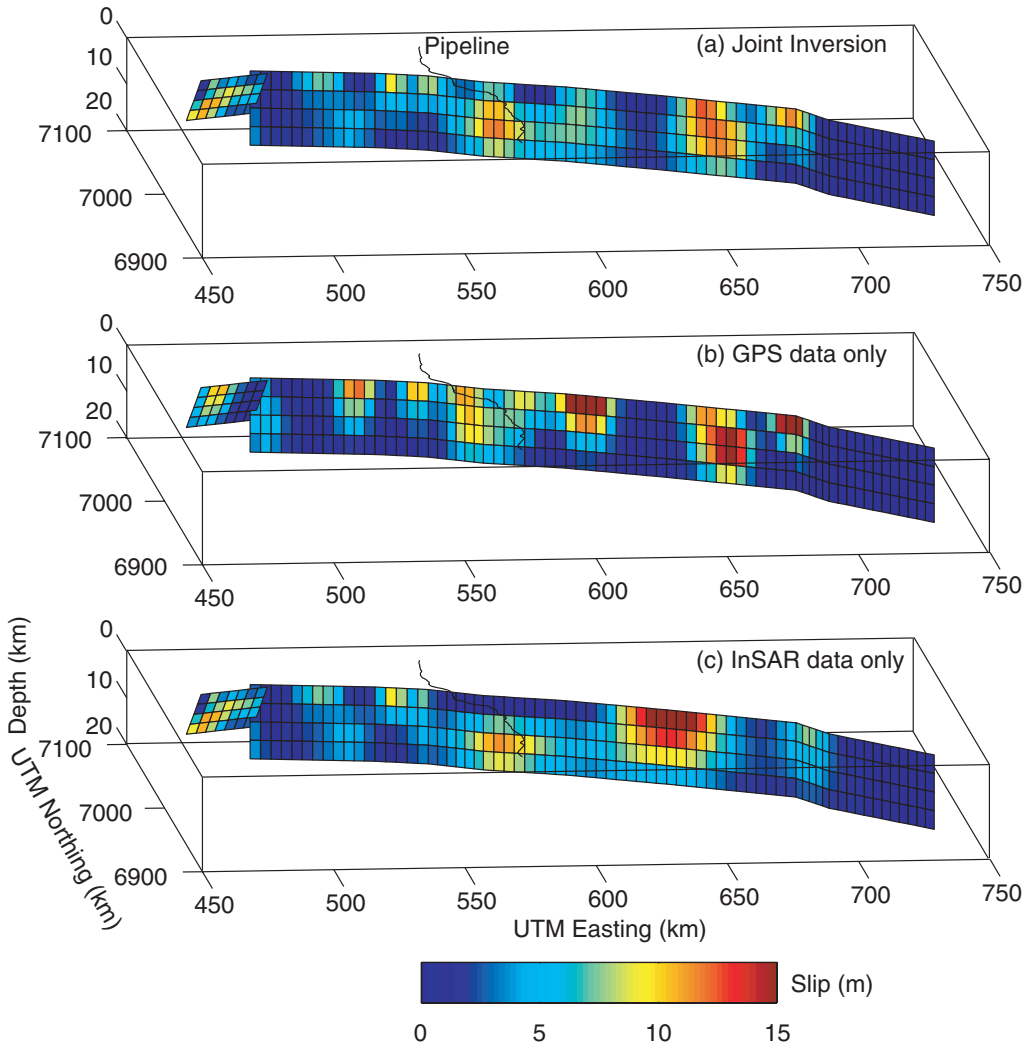

Figure 8. Three-dimensional representations of the distributed slip models. (a) Joint inversion solution; (b) GPS data only; (c) InSAR data only. The strike-slip fault extends from the surface to a depth of 16 km, and fault patches are ~4 by 4 km. The black line indicates the path of the pipeline. Coordinates are in UTM Zone 6.

By plotting ρ against the weighted misfit function Ω,

$$\Omega = \left\| \mathbf{W}\left(\mathbf{d} - (\mathbf{A}\ \mathbf{x}\ \mathbf{y}\ 1) \begin{pmatrix} \mathbf{m} \\ a \\ b \\ c \end{pmatrix} \right) \right\|_{L1}, \qquad (5)$$

a solution that has both low roughness and low misfit can be chosen (Fig. 7). In this case, the solution with a roughness of ~60 mm/km was selected (Fig. 8a). We repeated the inversion procedure twice, once excluding the InSAR data from the inversion (Fig. 8b), and once excluding the GPS data (Fig. 8c). In each case, we varied γ^2 in order to select a solution with a roughness of ~60 mm/km.

As for the 9-segment model, we determined errors for our nonlinear slip inversion using Monte Carlo simulation. These errors are then plotted on the fault plane and reveal locations where the slip models are poorly determined for each of the inversions (Fig. 9). For the InSAR-only inversion (Fig. 9c), 1-σ slip errors are generally less than 1 m everywhere west of the pipeline. East of the pipeline, because we have no InSAR data coverage, unsurprisingly the errors are very large. The exception is the eastern Totschunda fault, which has zero slip in every inversion, and therefore a formal error of zero. This reflects the poor resolution in this area and the zero-slip boundary condition. Zero-slip models will always be preferred if the data does not demand otherwise. The geodetic moment for the InSAR-only inversion was 700 $\pm$ 30 $\times$ 10^{18} N m.

The GPS-only inversion has a variable error distribution that depends very strongly on the distribution of the GPS observations. Where the two main GPS profiles cross the fault the slip errors are less than 0.5 m. In between these locations the errors, particularly for the near-surface fault

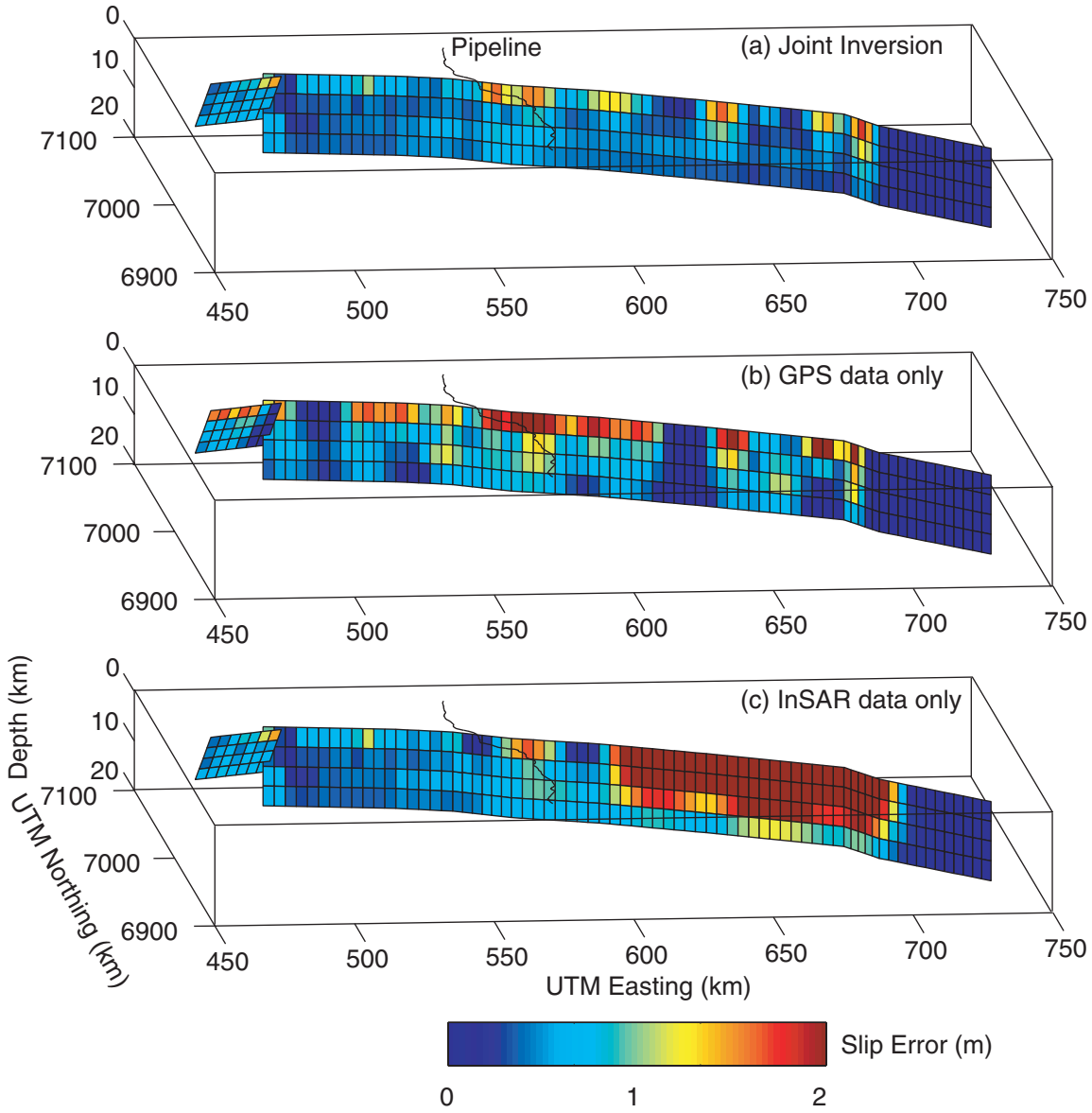

Figure 9. Three-dimensional representation of the uncertainties for the slip models shown in Figure 8. (a) Joint inversion solution; (b) GPS data only; (c) InSAR data only. Coordinates are in UTM Zone 6.

segments, are much larger, reaching more than 2 m in some places (Fig. 9b). The geodetic moment for the GPS-only inversion was $620 \pm 10 \times 10^{18}$ N m.

The joint inversion errors combine the best of the GPS-only and InSAR-only uncertainties (Fig. 9a). West of the pipeline crossing, the slip errors essentially look like the InSAR-only errors. East of the pipeline, the errors are nearly identical to those in the GPS-only inversion, although slightly smaller. In general, slip on shallow fault patches has larger uncertainties than slip on the deeper patches. The larger errors in the GPS-only inversion arise because less smoothing was required for the GPS-only inversion, compared to the InSAR-only and joint inversions, in order to obtain a model with the correct roughness.

The best-fit, joint-inversion slip model shows that the slip in the DFE varied considerably along strike. The model requires slip at depth of the Susitna Glacier fault to be considerably larger than the near-surface slip, with a maximum of ~11 m estimated by the inversion. On the main strike-slip fault, west of the pipeline crossing, the predicted slip is generally lower than 5 m. East of the pipeline, we find two main areas of high slip. The first, around 30 km east of the pipeline, has a maximum of ~12 m at a depth of 10 km, with slip of 7 ± 1 m at the surface. The second has even higher slip—our model predicts 12.5 ± 0.8 m at the surface. A third high-slip patch is shown in our slip model, near the junction of the Denali and Totschunda faults, but its 2-σ slip error is ~3 m, and so we do not place much confidence in

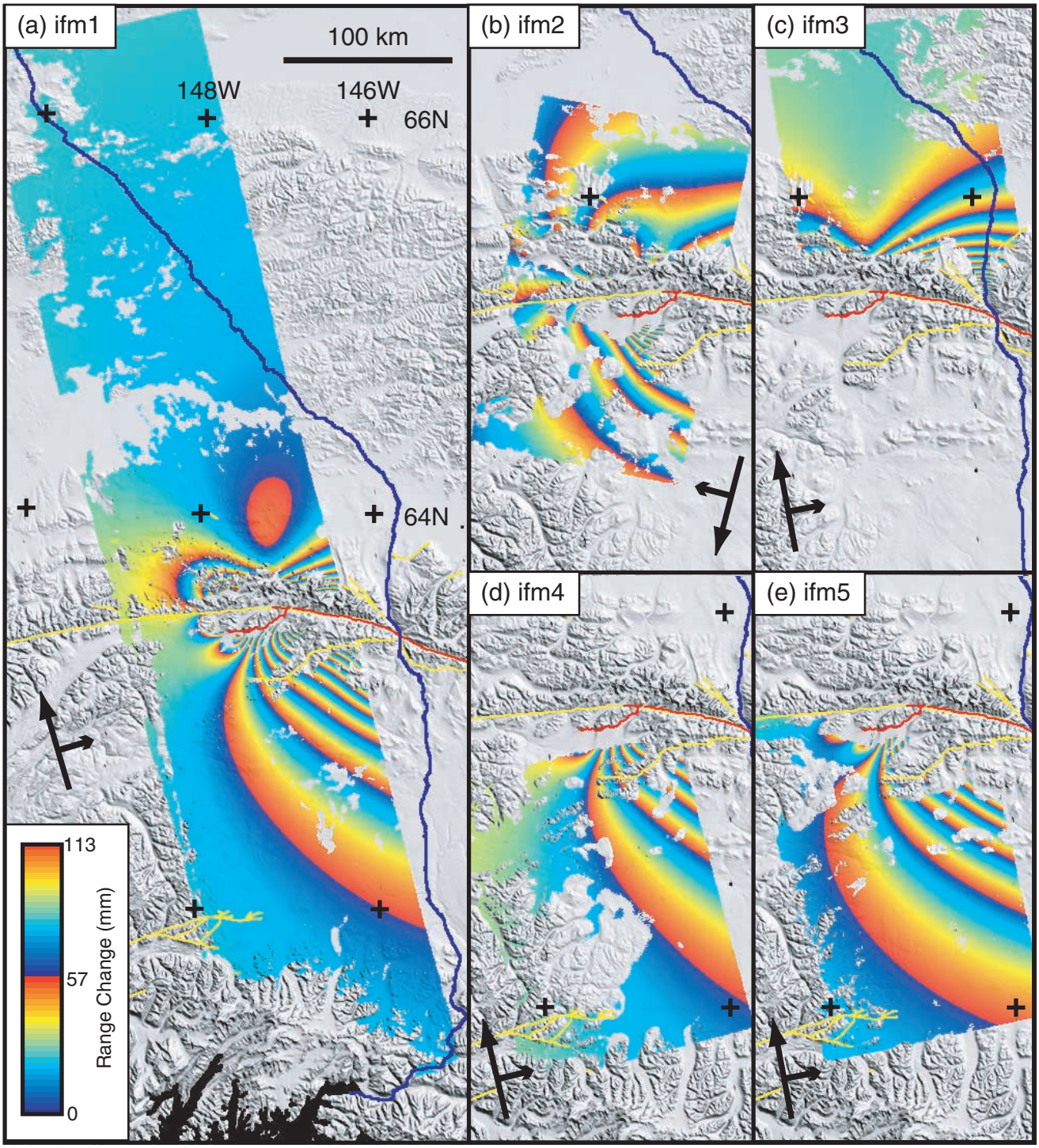

Figure 10. Synthetic interferograms generated by projecting the predictions of our joint-inversion, distributed-slip fault model into the satellite line of sight for each interferogram. All other features are as defined in Figure 2.

this result. The geodetic moment of the model is 670 ± 10 × 10^{18} N m (M_w 7.9), slightly larger than that of the nine-segment model, but still consistent with seismic estimates.

Synthetic interferograms (Fig. 10) match the observations well and the residuals (Fig. 11) are small—the rms misfit for the InSAR data is reduced from 3.1 cm to 2.4 cm. The GPS data have a much improved fit to the distributed slip model compared to the nine-segment model (Fig. 6); the rms misfit for the horizontal components is reduced from 8.4 to 1.5 cm, and the vertical rms is down from 5.4 to 3.0 cm.

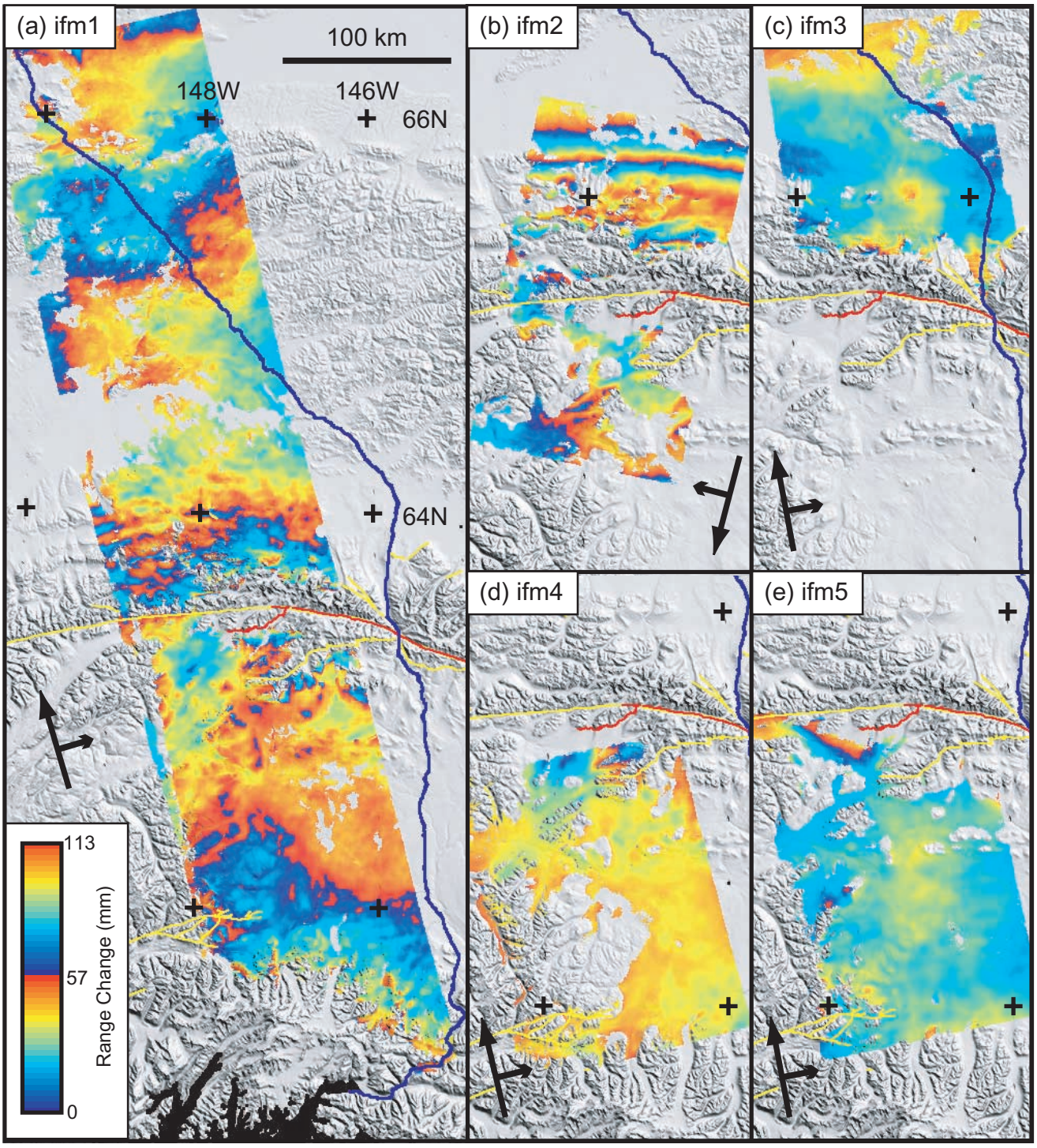

Figure 11. Residual interferograms for our distributed-slip model, generated by subtracting the model interferograms (Fig. 10) from the observed data (Fig. 2). Estimated linear orbital ramps have been removed. Other features are as defined in Figure 2.

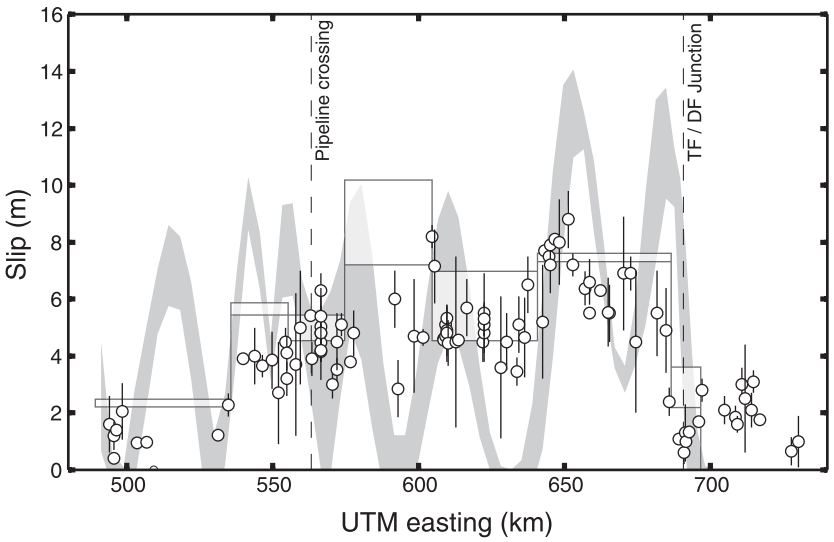

Figure 12. Comparison of surface slip observations on the Denali fault (white circles with bars indicating 95% confidence limits where known) with predictions of our geodetic data inversions. The gray band is the 95% confidence bound on the slip in the upper 4 km determined by our distributed-slip model (Fig. 8). White bars are the 95% bounds on slip in the nine-segment model. The most eastern segment, along the Totschunda fault, has zero slip in this inversion. Coordinates are in UTM Zone 6.

We also compared the best-fit distributed and nine-segment slip models with the surface slip observations presented by Haeussler *et al.* (2004) to provide independent verification of our model results (Fig. 12). For the most part, the agreement is reasonable to within the respective errors of the individual data sets. However, the peak slip predicted by the distributed slip model of 12.5 $\pm$ 0.8 m (UTM Easting 650 km) is larger than the peak slip observed at the surface of 8.8 $\pm$ 0.5 m, although they are located in the same place. It is possible that the discrepancy reflects a genuine difference between surface slip and the average slip in the upper four kilometers of crust. Alternatively, because the high slip is required to fit the near-fault GPS displacements observed at MEN, the discrepancy may be due to the exact fault geometry chosen in this location, local heterogeneities in elastic structure near MEN, or the choice of smoothing parameter and data weightings in the inversion scheme. We note that Hreinsdóttir *et al.* (2003) also found a similar pattern of high slip in this location; although their peak surface slip was around 11 m, they estimated ~15 m of slip at depth. In experiments where we varied the amount of smoothing, we could not reduce the peak slip, except for inversions with a very high degree of smoothing, which had poor fits to the data. The slip in our nine-segment model, which essentially averages the slip observed in the distributed model both down-dip and along strike, has a much closer fit to the surface offsets, but does not match the GPS displacements well. Our three main areas of moment release—the SGF, the area just east of the pipeline crossing, and the area near the peak observed surface slip—also concur with observations drawn from seismic data (e.g., Eberhart-Phillips *et al.*, 2003; Tsuboi *et al.*, 2003; Dreger *et al.*, 2004) although the details differ.

Conclusions

We have presented new geodetic data from Radarsat-1 interferometry and used it in conjunction with GPS data to determine a slip model for the 3 November 2002 DFE. The combination of ascending and descending InSAR data provides a powerful constraint on the slip distribution and fault geometry of the western end of the earthquake. In particular, we are able to place tight bounds on the geometry of the SGF slip, which initiated the earthquake.

Although we have also been able to determine a distributed slip model, the lack of proximal GPS and InSAR data for much of the rupture length means that the uncertainties in the model are large, particularly near the surface. Despite the large archive of SAR scenes at the Alaska SAR Facility, we have been unable to form coherent interferograms for the eastern half of the earthquake rupture. In an area such as this, where short interval interferograms are required to maintain good coherence with C-band radar, it is essential that acquisitions of both ascending and descending data are made whenever possible, preferably on every satellite pass. We recognize that this may not occur without a dedicated geodetic InSAR mission.

Acknowledgments

T.J.W. is supported by a NERC postdoctoral research fellowship. Radarsat-1 images are © 2002 Canadian Space Agency and were provided by the Alaska SAR Facility (ASF). Part of this research was performed at the SAIC, EROS Data Center under USGS Contract No. O3CRCN0001 and funding from NASA (NRA-99-OES-10 RADARSAT-0025-0056). We thank J. Laurencelle, V. Wolf, and other ASF staff members for their special efforts in making the SAR data available to us, Sigrún Hreinsdóttir for access to the GPS data, and Tim Dawson for providing us with the latest field observations. We thank Wayne Thatcher, Jim Savage, and two anonymous referees for comments that helped improve the manuscript. Some figures were prepared using the public domain Generic Mapping Tools (Wessel and Smith, 1998).

References

Anderson, G., and C. Ji (2003). Static stress transfer during the 2002 Nenana Móuntain–Denali fault, Alaska, earthquake sequence, *Geophys. Res. Lett.* **30,** doi 10.1029/2002GL016724.

Bamler, R. (1992). A comparison of range-doppler and wavenumber domain SAR focusing algorithms, *IEEE Trans. Geosci. Remote Sensing* **30,** 706–713.

Bro, R., and S. De Jong (1997). A fast non-negativity-constrained least squares algorithm, *J. Chemometrics* **11,** 392–401.

Bürgmann, R., P. Rosen, and E. Fielding (2000). Synthetic aperture radar interferometry to measure Earth's surface topography and its deformation, *Ann. Rev. Earth. Planet. Sci.* **28,** 169–209.

Dreger, D., D. Oglesby, R. Harris, N. Ratchkovski, and R. Hansen (2004). Kinematic and dynamic rupture models of the November 3, 2002 M_w Denali, Alaska, earthquake, *Geophys. Res. Lett.* **31,** L04,605, doi 10.1029/2003GL018333.

Eberhart-Phillips, D., P. Haeussler, J. Freymueller, A. Frankel, C. Rubin, P. Craw, N. Ratchkovski, G. Anderson, A. Crone, T. Dawson, H. Fletcher, R. Hansen, E. Harp, R. Harris, D. Hill, S. Hreinsdóttir, R. Jibson, L. Jones, D. Keefer, C. Larsen, S. Moran, S. Personius, G. Plafker, B. Sherrod, K. Sieh, and W. Wallace (2003). The 2002 Denali fault earthquake, Alaska: a large magnitude, slip-partitioned event, *Science* **300,** 1113–1118.

Fuis, G., and L. Wald (2003). Rupture in South-Central Alaska—the Denali fault earthquake of 2002, *USGS Fact Sheet 014-03.*

Gamma Remote Sensing Research and Consulting AG, Switzerland, Gamma modular SAR processor (2003). Available at www.gamma-rs.ch (last accessed December 2004).

Haeussler, P., D. Schwartz, T. Dawson, H. Stenner, J. Lienkaemper, B. Sherrod, F. Cinti, P. Montone, P. Craw, A. Crone, and S. Personius (2004). Surface rupture and slip distribution of the Denali and Totschunda faults in the 3 November 2002 **M** 7.9 earthquake, Alaska, *Bull. Seism. Soc. Am.* **94,** no. 6B, S25–S52.

Hanssen, R. (2001). *Radar Interferometry: Data Interpretation and Error Analysis,* Kluwer Academic Publishers, Dordrecht, Netherlands.

Hreinsdóttir, S., J. Freymueller, H. Fletcher, C. Larsen, and R. Burgmann (2003). Coseismic slip distribution of the 2002 M_w 7.9 Denali fault earthquake, Alaska, determined from GPS measurements, *Geophys. Res. Lett.* **30,** 1670, doi 10.1029/2003GL017,447.

Jónsson, S., H. Zebker, P. Segall, and F. Amelung (2002). Fault slip distribution of the 1999 M_w 7.1 Hector Mine earthquake, California, estimated from satellite radar and GPS measurements, *Bull. Seism. Soc. Am.* **92,** 1377–1389.

Joughin, I. (2002). Ice sheet velocity mapping: a combined interferometric and speckle tracking approach, *Ann. Glaciol.* **34,** 195–201.

Lu, Z., T. J. Wright, and C. Wicks (2003). Deformation of the 2002 Denali fault earthquakes, Alaska, mapped by Radarsat-1 interferometry, *EOS* **84,** 425, 430–431.

Massonnet, D., and K. L. Feigl (1998). Radar interferometry and its application to changes in the earth's surface, *Rev. Geophys.* **36,** no. 4, 441–500.

Menke, W. (1989). *Geophysical Data Analysis: Discrete Inverse Theory,* Revised Ed., Academic Press, San Diego.

Okada, Y. (1985). Surface deformation due to shear and tensile faults in a half-space, *Bull. Seism. Soc. Am.* **75,** 1135–1154.

Parashar, S., E. Langham, J. McNally, and S. Ahmed (1993). RADARSAT mission requirements and concept, *Can. J. Remote Sensing* **19,** 280–288.

Strang, G., and K. Borre (1997). *Linear Algebra, Geodesy, and GPS*, Wellesley-Cambridge Press, Wellesley, Mass.

Tsuboi, S., D. Komatitsch, C. Ji, and J. Tromp (2003). Broadband modeling of the 2002 Denali fault earthquake on the Earth Simulator, *Phys. Earth Planet. Interiors* **139,** 305–312.

Wessel, P., and W. H. F. Smith (1998). New, improved version of generic mapping tools released, *EOS* **79,** 579.

Wright, T. J. (2002). Remote monitoring of the earthquake cycle using satellite radar interferometry, *Phil. Trans. R. Soc. Lond. A* **360,** 2873–2888.

Wright, T. J., B. Parsons, J. Jackson, M. Haynes, E. Fielding, P. England, and P. Clarke (1999). Source parameters of the 1 October 1995 Dinar (Turkey) earthquake from SAR interferometry and seismic bodywave modelling, *Earth Planet. Sci. Lett.* **172,** 23–37.

Wright, T. J., Z. Lu, and C. Wicks (2003). Source model for the M_w 6.7, 23 October 2002, Nenana Mountain Earthquake (Alaska) from InSAR, *Geophys. Res. Lett.* **30,** 1974, doi 10.1029/2003GL018,014.

Centre for the Observation and Modelling of Earthquakes and Tectonics
Department of Earth Sciences
Parks Road, Oxford, OX1 3PR, United Kingdom
tim.wright@earth.ox.ac.uk
(T.J.W.)

U.S. Geological Survey
EROS Data Center
SAIC, 47914, 252nd St.
Sioux Falls, South Dakota 57196
lu@usgs.gov
(Z.L.)

U.S. Geological Survey
Earthquake Hazards Program
345 Middlefield Road, MS-977,
Menlo Park, California 94025
cwicks@usgs.gov
(C.W.)

Manuscript received 10 March 2004.